PERGAMON

Energy Conversion & Management 41 (2000) 249–280

ENERGY CONVERSION & MANAGEMENT

www.elsevier.com/locate/enconman

Local design, testing and manufacturing of small mixed airfoil wind turbine blades of glass fiber reinforced plastics Part I: Design of the blade and root

S.M. Habali[a,*], I.A. Saleh[b]

[a]*Mechanical Engineering Department, Faculty of Engineering and Technology, University of Jordan, Amman, Jordan*
[b]*Renewable Energy Center, Royal Scientific Society, Amman, Jordan*

Received 27 October 1998; accepted 16 May 1999

Abstract

Wind energy has attracted a great deal of attention in recent years in Jordan as one of the possible alternative renewable energy resources. Almost of the local research and development activities in this field were directed to explore, develop, and optimal utilization of energy systems. The time has come to establish a link between local scientific (academic) work and local industries to produce a usable technology which will increase the local share in an inevitably emerging wind energy industry in Jordan. To achieve this goal, a well founded manufacturing base is required. The most important component of a Wind Energy Converter is the rotor. The efficiency of a rotor is characterized by its profile (airfoil section) and the corresponding aerodynamic design. A selection procedure of airfoil section and the aerodynamic design of the blade for a small wind turbine are discussed and implemented in this paper (Part I). It is found that for small blades up to 5 m long, two different air foils mixed at the outer third of the span will be sufficient and demonstrated good strength and aerodynamic characteristics. As a composite material, the Glass Fiber Reinforced Plastic was used in designing the rotor blade. This rotor was then installed on 15 kW grid-connected-pitch-controlled machine. A static proof load test indicated that this blade could withstand loads ten times the normal working thrust, and a field performance test showed that the rotor blade has a 41.2% measured average power coefficient.

Keywords: Mixed airfoil blades of CM; Mixed airfoil blades of GRP; Mixed airfoil blades rotor of GRP; Design of mixed airfoil-blades rotor of GRP

Abbreviations: CM, Composite Materials; GRP, Glass Fiber Reinforced Plastics.

* Corresponding author.
E-mail address: habali@fet.ju.edu.jo (S.M. Habali)

0196-8904/00/$ - see front matter
PII: S0196-8904(99)00103-X

Nomenclature

A_z	Blade-cross sectional area perpendicular to z axis (blade axis)
a	Axial interface factor
a'	Tangential interface factor
B	Number of blades
L	Lift force
D	Drag force
C_{D}	Drug coefficient
C_{L}	Lift coefficient
C_m	Moment coefficient
C_x	Force coefficient in x direction
C_y	Force coefficient in y direction.
c	Chord length
d	Diameter
d_{i}	Inside diameter
d_{o}	Outside diameter
E	Modulus of elasticity
F	Circulation reduction factor
Γ	Circulation of one blade at radius r
Γ_∞	Circulation of rotor with infinite number of blades
F_{c}	Centrifugal force
F_x	Force component in x direction
F_y	Force component in y direction
F_z	Force component in z direction
F_{t}	Tangential force
m_x	Bending moment about x axis
m_y	Bending moment about y axis
f	Tip losses factor, Line frequency
G	Shear modulus
I_x	Area moment of inertia around x axis.
I_y	Area moment of inertia around y axis
I_z	Area moment of inertia around the z axis (polar moment of inertia)
m	Time rate of change of air mass
P	Power
C_p	Power coefficient
p	Ambient pressure
Q	Torque
R	Total radius
r	Local radius
T	Thrust force
U	Local wind velocity

V	Wind speed velocity
α	Angle of attack
α_t	Angle of attack of blade tip
β	Twist angle of blade
η	Efficiency
λ	Tip speed ratio of rotor blade
Φ	Flow angle of relative wind speed to the airfoil
Φ_t	Flow angle of relative wind speed to the airfoil tip
Ω	Angular speed of rotor
ω	Angular speed of wake
ρ	Density of air
σ	Magnitude of stress
ε	Magnitude of strain
L_b	Length of blade
FEM	Finite Element Method
r_{cm}	Blade center of mass measured from the root
GRP	Glass Fiber Reinforced Plastic
3D	Three dimensional
SERI	Solar Energy Research Institute.
NACA	National Advisory Committee of Aeronautics.
WEC	Wind Energy Converter

1. Introduction

In order for a wind energy industry to be established in Jordan, a founded manufacturing base is required. Jordan has virtually hundreds of different kinds of industries, but no one is specialized in manufacturing wind system components. Thus, a problem exists which will be addressed in this paper to establish a local manufacturing procedure and capability for Glass Fiber Reinforced Plastic (GRP) wind turbine blades and to identify the basic components of this technology which are required from the local market.

Wind turbine blades must be designed to operate in the most unpredictably severe environmental conditions and still give satisfactory performances for the lifetime of the system. Rotor blade design relies heavily on aerodynamic theory, since the blade is an aerodynamic body having special geometry characterized mainly by an airfoil cross section. Extensive calculations will be necessary in order to determine the blade parameters, such as chord, thickness and twist distributions and taper, that are matched with the selected airfoil section. A brief summary of rotor blade design is, therefore, given to define the various parameters governing blade design and with the help of a special software, a complete aerodynamic analysis was performed. A three-dimensional (3D) solid model is then created and a FEM analysis was performed using a powerful computer which yielded a simulation to the actual blade operating under loads. A final blade was verified and a full scale model was made.

For practical purposes, more than one airfoil section must be chosen to fit the thickness distribution where, closer to the root, a thick section is needed for structural reasons, and thinner sections are used along the outboard region with a smooth transition from root to tip. One of the objectives of this research work is to develop the basic engineering design of GRP blades and also to establish the procedure for the local manufacturing. Ultimately, this work will contribute toward the initiation of a GRP blade test facility which can lead to establishing a local design code.

Much computer software has been written to simulate what happens in reality during the rotor blade flight and to attempt to predict the resulting aerodynamic loads and their variations. For example, Harten [1] used a software package called loads that analyzes blade loads for rigid rotors of simple geometry for the Grumman WS33 wind turbine and calculated that the sensitivity of the load predictions to the phase of the turbulent wind simulation record stressed the need for improving wind simulation techniques. The blades are designed and constructed to withstand loads resulting from normal operation, gusts, or turbulence, which induce major alternating stresses, and therefore, the material used (GRP) must be capable of resisting the fatigue resulting from them. In this context, a variety of blade designs were suggested by Park [2], but more advanced blades having optimized geometry were introduced by Jackson et al. [3]. In general, the design of a wind turbine rotor consists of two steps, as given by Lysen [4]:

1. the choice of basic parameters: type of airfoil, tip speed ratio and
2. calculations of the setting angles and chord length at different positions along the blade.

One of the most recent developments in blade design, which was consulted during this study, is the special purpose thin airfoil family introduced by Tangler et al. [5] through the solar energy research institute (SERI), Golden, Colorado. These SERI blades were described by Davidson [6] as 'the blades of the future' and could produce 31% more power than the traditional Danish made blades. Most modern blades, however, have profiles of the NACA 63nnn series. These profiles have shown excellent properties for wind turbine blades, but some improvements can still be achieved in the profiles in the inner portion of the blades in order to make the profile sufficiently thick while still having high lifting force. For this reason, developments are proceeding to design thick airfoils for the in board region of rotor blades. An example of this is the SERI S897 profile. Other examples are: the LS(1)-0421 and the NACA 63-621 profiles. It is interesting to notice the big difference among these profiles; however all are suited for use.

During the course of this work, one Jordanian company was identified and has succeeded in adapting to this new technology and, according to the procedure set forth, had produced a high quality 5 m GRP blade. The blade has also passed successfully the pre-assigned stress test and, when installed on a functional wind turbine, performed satisfactorily with a favorable power coefficient of 41.2%.

2. Design of the rotor blade

2.1. Blade size and material

The philosophy underlying the choice of the blade size was that a small blade will be too stiff by nature and unable to exhibit the behavior of full size blades used for electricity

generation. On the other hand, a large blade will exceed the capabilities of the technical and financial resources. Hence, the decision was made to experiment with a 5 m long blade which has the characteristics of large blades and the handling convenience of small blades.

The choice of the material based on some considerations, such as the material weight and strength besides it's availability in Jordan, so that it can be adapted to mass production. This choice of the GRP can be related to many attributes, one of which is the availability of the polyester resin which is locally produced.

2.2. Blade shape and profile

2.2.1. Aerodynamic theory

2.2.1.1. Overview of rotor blade aerodynamics. Rotor blade design relies heavily on aerodynamic theory. The blade is an aerodynamic body having a special geometry mainly characterized by an airfoil cross section. Extensive calculations are necessary to determine the blade parameters, such as chord, thickness and twist distributions over the blade length and taper that are matched with the selected airfoil sections. For practical purposes, more than one airfoil section must be chosen to fit the thickness distribution, where the thickness decreases with the radius of the rotor (blade length) and a smooth transition condition is satisfied.

The flight of a rotor blade is a complex phenomenon which can not be modeled exactly. This complexity arises from the fact that the flow of the air around the blade is 3D with various vortex sheddings, resulting from the variable rotational speed. This is also coupled with the variation of wind speed distribution along the blade caused by the wind shear and the large scale boundary layer on the earth surface. This phenomenon, however, can be approximately described by imposing several assumptions. One of the simplest descriptions of extracting energy from the wind is the one dimensional, incompressible, non-viscous flow model using the axial momentum theory, including the rotational wake effects. More recently, Wilson and Lissaman [7] have analyzed the aerodynamic performance of wind turbines.

The momentum theory cannot provide the necessary information on how to design the rotor blades. However, the momentum theory when combined with the blade element theory will then yield this kind of information.

2.2.1.2. The axial momentum theory. Three principal assumptions are made:

- the flow is completely axial,
- the flow is rotationally symmetric, and
- no friction occurs when the air passes the wind turbine rotor.

From Fig. 1 we obtain:

- the continuity equation:

$$UA = U_1 A_1 \tag{1}$$

- momentum (thrust) equation:

$$T = \dot{m}(V - U_1) = \rho A U (V - U_1) \tag{2}$$

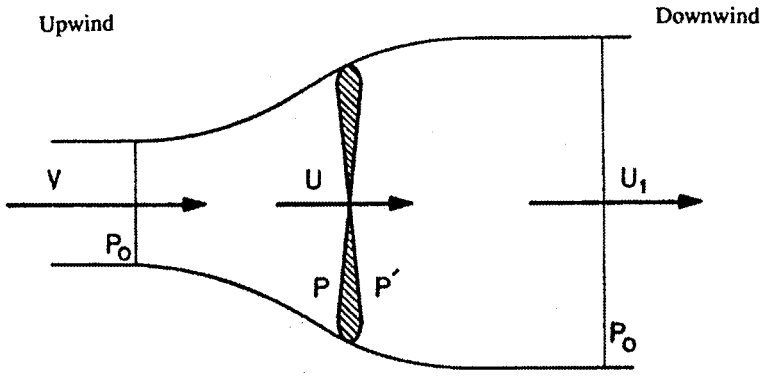

Fig. 1. Axial flow model.

- Bernoulli upwind

$$p_0 + 0.5\rho V^2 = p + 0.5\rho U^2 \tag{3}$$

- Bernoulli downwind

$$p_0 + 0.5\rho U_1^2 = p' + 0.5\rho U^2 \tag{4}$$

Thus,

$$\Delta p = p - p' = 0.5\rho\left(V^2 - U_1^2\right) \tag{5}$$

Combining Eqs. (2) and (5) with

$$T = A\Delta p \tag{6}$$

yields

$$U = 0.5(V + U_1) \tag{7}$$

The power extracted will then be:

$$P = 0.5\dot{m}\left(V^2 - U_1^2\right) = 0.5\rho UA\left(V^2 - U_1^2\right) \tag{8}$$

Now, denoting a power coefficient by

$$C_p = \frac{P}{0.5\rho V^3 A} \tag{9}$$

and knowing that the flow has been retarded at the rotor disc by slowing down a certain amount a, then we get:

$$U = (1 - a)V \tag{10}$$

Eqs. (7) and (10) give

$$U_1 = (1 - 2a)V \tag{11}$$

Substituting Eqs. (10) and (11) into Eq. (8) and the result into Eq. (9) gives the power coefficient of

$$C_p = 4a(1 - a)^2 \tag{12}$$

which has a maximum when $a = 1/3$, as shown in Fig. 2.

In order to enhance the results and make them close to reality, the effect of wake rotation will be included. In describing this effect, the assumption is made that upstream of the rotor, the flow is entirely axial and that the flow downstream rotates with an angular velocity ω, but remains irrotational.

Expressions for torque and power may be obtained by considering the flow through an annulus at radius r with area

$$\mathrm{d}A = 2\pi r\,\mathrm{d}r \tag{13}$$

By changing the momentum in the air in the tangential direction, tangential forces F_t act upon the rotor as:

$$\mathrm{d}F_t = \dot{m}\,\mathrm{d}V = \rho U\,\mathrm{d}A\omega r \tag{14}$$

Substitute Eq. (13) into Eq. (14) we obtain

$$\mathrm{d}F_t = 2\pi\rho U\omega r^2\,\mathrm{d}r \tag{15}$$

The torque generated in the annulus dr is:

$$\mathrm{d}Q = 2\pi\rho U\omega r^3\,\mathrm{d}r \tag{16}$$

and since

$$P = Q\omega \tag{17}$$

the power extracted is

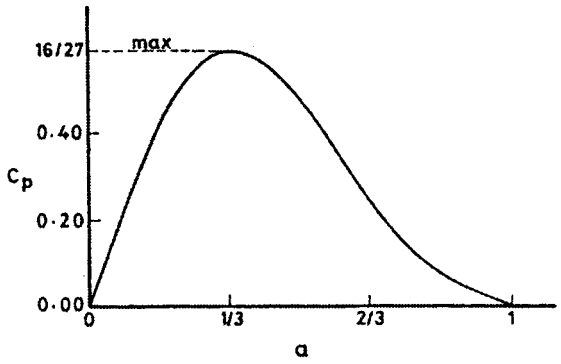

Fig. 2. Power coefficient — axial interference factor curve.

$$dP = 2\pi\rho\Omega U\omega r^3\, dr \tag{18}$$

The total torque and the power of the rotor become

$$Q = 2\pi\rho \int U\omega r^3\, dr \tag{19}$$

and

$$P = 2\pi\rho\Omega \int U\omega r^3\, dr \tag{20}$$

In order to be able to calculate torque and power, one must have the values of the wake's angular velocities ω by introducing the tangential induction factor a' [6] as:

$$a' = \frac{0.5\omega}{\Omega} \tag{21}$$

2.2.1.3. Blade element theory. Two main assumptions govern this theory:

- The forces and the moments acting on a blade element are solely due to the lift and drag characteristics of the profile section of that blade element.
- There should be no interference between adjacent blade elements because the forces on each element are calculated with their local wind velocities. The flow around the blade element (of length dr) at radius r may be considered as a two-dimensional flow as shown in Fig. 3. In this representation, the angular velocity Ω of the rotor is assumed to have the value of the final rotational velocity ω in the wake, [4], which is an approximation to Eq. (21) by setting $a' = 1$.

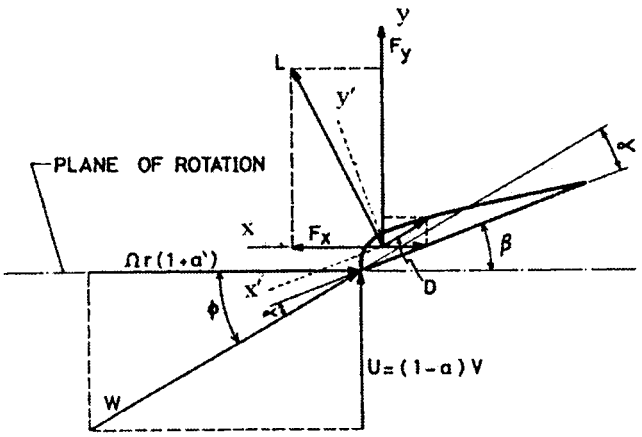

Fig. 3. Velocity and forces at a blade element at radius r.

Defining

$$\mathrm{d}q = 0.5\rho W^2\,\mathrm{d}A = 0.5\rho W^2 c\,\mathrm{d}r \tag{22}$$

gives:

$$C_\mathrm{L} = \frac{\mathrm{d}L}{\mathrm{d}q} \tag{23}$$

$$C_\mathrm{D} = \frac{\mathrm{d}D}{\mathrm{d}q} \tag{24}$$

$$C_x = \frac{\mathrm{d}F_x}{\mathrm{d}q} \tag{25}$$

and

$$C_y = \frac{\mathrm{d}F_y}{\mathrm{d}q} \tag{26}$$

The following trigonometric relations may be obtained from Fig. 3:

$$\alpha = \Phi - \beta \tag{27}$$

$$\tan\Phi = \frac{(1-a)\mathrm{V}}{(1+a')\Omega r} \tag{28}$$

$$C_y = C_\mathrm{L}\cos\Phi + C_\mathrm{D}\sin\Phi \tag{29}$$

$$C_x = C_\mathrm{L}\sin\Phi - C_\mathrm{D}\cos\Phi \tag{30}$$

Expressions for the thrust, $\mathrm{d}T$, and the torque, $\mathrm{d}Q$, for an element $\mathrm{d}r$ at radius r can now be derived as follows:

$$\mathrm{d}T = BC_y\,\mathrm{d}q = BC_y 0.5\rho W^2 c\,\mathrm{d}r \tag{31}$$

and

$$\mathrm{d}Q = BC_x\,\mathrm{d}qr = BC_x 0.5\rho W^2 cr\,\mathrm{d}r \tag{32}$$

where B is the number of blades.

The thrust and torque equations were also derived using the axial moment theory, but with the assumption that no friction occurs. Hence, in order to equate the two results, we must assume $C_\mathrm{D} = 0$, then equating Eq. (2) to Eqs. (31) and (16) to Eq. (32) gives:

$$\frac{a}{1-a} = \frac{cBC_y}{8\pi r\sin^2\Phi} \tag{33}$$

and

$$\frac{a'}{1+a'} = \frac{cBC_x}{8\pi r \sin\Phi\cos\Phi} \tag{34}$$

From Fig. 3 we can conclude that:

$$W = \frac{U}{\sin\Phi} = \frac{V(1-a)}{\sin\Phi} \tag{35}$$

or

$$W = \frac{\Omega r(1+a')}{\cos\Phi} \tag{36}$$

The local solidity ratio of the rotor is defined as:

$$\sigma = \frac{cB}{2\pi r} \tag{37}$$

Solving Eqs. (33) and (34) for a and a', respectively, gives:

$$a = \frac{1}{\left(4\sin^2\Phi/\sigma C_y\right)+1} \tag{38}$$

and

$$a' = \frac{1}{(4\sin\Phi\cos\Phi/\sigma C_x)-1} \tag{39}$$

With a finite number of blades (e.g. $B = 3$), the assumption that the flow through the rotor is rotationally symmetric obviously does not hold, in addition to the dimensional flow assumption. The effects due to the finite number of blades results in the performance losses concentrated near the tip of the blade. This phenomenon, known as the tip losses model, was first analyzed by Prandtl [8]. The tip losses are expressed by a circulation reduction factor defined by:

$$F = \frac{B\Gamma}{\Gamma_\infty} = \frac{2}{\pi a r\cos(e^{-f})} \tag{40}$$

where Γ is the actual circulation of one blade at radius r, and Γ_∞ is the circulation of a rotor with an infinite number of blades as was calculated in the axial momentum theory, and

$$f = \frac{(B/2)(R-r)}{r\sin\Phi} \tag{41}$$

Prandtl [13] gives, as a result, the modified axial and tangential velocity factors:

$$a = \frac{1}{(4\sin^2\Phi)F/\left(\sigma C_y\right)+1} \tag{42}$$

and

$$a' = \frac{1}{(4\sin\Phi\cos\Phi)F/(\sigma C_x) - 1} \tag{43}$$

Note that the Prandtl factor F does not change the relation between the two factors as previously derived.

3. Airfoil selection

Airfoils chosen for wind turbine applications have focused on the half century old NACA 23nnn and NACA 44nn airfoil series. The NACA 23nnn series were found by Tangler [5], to experience a large drop in maximum lift coefficient, $C_{L,max}$, as the airfoil becomes solid (dirty). This problem was also found on the NACA 44nnn series, however to a lesser extent.

In an effort to solve this blade soiling problem, manufacturers began using the LS-1 and NACA 63nnn series of airfoils. Both of these airfoil sections have their camber further back which provides some improvement in reducing the airfoil's $C_{L,max}$ sensitivity to roughness effects. In addition, the NACA 63nnn provided a lower $C_{L,max}$ which helped control peak power. However, this characteristic is desirable only over the tip region of the blade, and when used on the inboard region, a degradation in energy production is expected. The LS-1 series have the opposite problem. This airfoil provides a desirable high $C_{L,max}$ toward the blade root but contributes to excessive peak power when used over the outboard portion of the blade. The excessive peak power must then be controlled, with undesirable reduction in blade solidity or a less efficient blade operating pitch angle. Fig. 4a shows the two airfoil profiles: LS(1)-0421 and NACA 63-621.

The FX-S airfoil family has in it's series the characteristics required for the outboard region and also the tip. This family has a stable lift coefficient (C_L) at high angles of attack (low wind speed). In addition, their moment coefficient, C_m, is smooth and almost constant over the whole range of operating angles of attack [9]. The airfoil FX66-S-196, shown in Fig. 4b, will be selected for the outboard region of our blade.

The inboard region of the blade must be thicker and have more material to withstand the higher stresses and also have a smoother geometry transition to the circular connecting flange at the root. The NACA 63-621 profile, shown in Fig. 4a, is selected for the inboard region which has these characteristics and is very similar to the FX 66- S-196 profile. In addition, the profile similarities will simplify the transition from the inner to outer board regions.

4. Determination of the blade data

The design and construction of sophisticated wind turbine blades requires enormous amounts of data. Most important are those describing the geometry and structural characteristics of the blade, such as length (radius of the rotor), thickness distribution, chord length distribution, twist, root connection, etc.

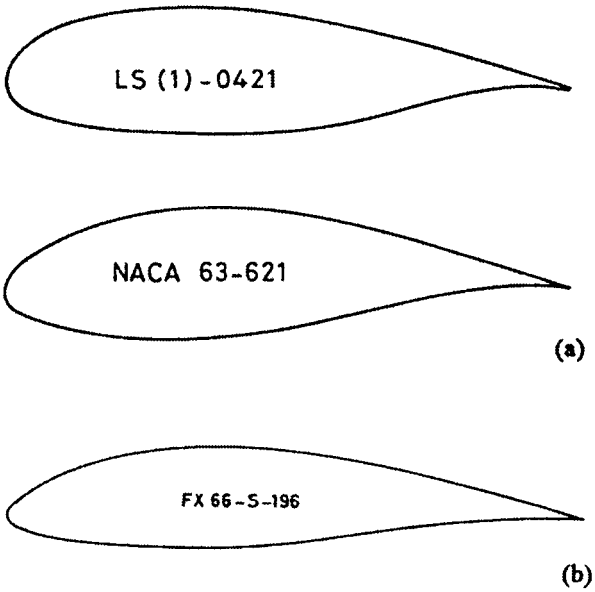

Fig. 4. Profiles acceptable for use by mixed wind turbine blades: (a) on inboard region of the blade, and (b) on outboard region of blade.

4.1. Radius of the rotor

The radius of the rotor, i.e. the length of the rotor's blade, can be determined from the rotor's area which depends in it's value on the rated power of the wind turbine. The rated power can be calculated from the equation

$$P_{\text{rat}} = 0.5\rho V_{\text{rat}}^3 A C_{p,\text{rat}} \tag{44}$$

The first step is to identify the output capacity of the proposed wind turbine. This is an open decision that depends on the needs and desires of the investor who wants to build the wind machine. The rated power, P_{rat}, could range from a few hundred Watts to the order of Megawatts.

In our case, the rated power is taken at 20 kW. The rated power is only defined for pitch controlled machines at one value of wind speed and power coefficient. These two values can be chosen by experience and will directly influence the size of the wind turbine rotor, i.e. the diameter. There are some theoretical bases for choosing the rated wind speed for a given wind turbine [10]. However, experience has shown that most machines have a rated speed around 10 m/s ($V_{\text{rat}} \cong 10$ m/s) and for small fast running machines lower values can be realized. Hence, for this design, $V_{\text{rat}} = 9.5$ m/s is selected.

The maximum power coefficient attained for an ideal wind turbine is $C_{p,\max} = 16/27 = 59\%$, as was previously shown in Fig. 2. Also, from manufacturer data and test results of Ta'ani et al. [11], most machines of this size operate at $C_p \cong 0.4(= 40\%)$, which is chosen for this design. Furthermore, for this design, the air density is selected as $\rho = 1.25$ kg/m^3.

With the previous parameters selection, the only remaining unknown is the rotor's area that can be calculated from Eq. (44) as: $A = P_{rat}/(0.5\rho V_{rat}^3 C_{p,rat}) = 20000/(0.5 \times 1.25(9.5)^3 0.4) = 93.3$ m^2, and the diameter of the rotor will be $d = (4A/\pi)^{0.5} = 10.9$ m.

4.2. Dimensions of rotor

The wind turbine rotor usually consists of two main components, hub and blades, as shown in Fig. 5. The hub can be rigid in the case of fixed pitch, or can have rotating flanges for variable pitch machines, as in our case. The hub and flange, including axle assembly, is assigned a radius of 0.45 m, leaving the rotor blade to be 5 m long from flange to tip as shown in Fig. 5.

4.2.1. Root of The blade

The blade root is the heaviest and the thickest part of the blade because it carries the blade structure and it is the junction point between the blade body and the hub as shown in Fig. 5. The root has to resist the maximum moments and torques transmitted by the aerodynamic forces through the blade to the rotor shaft, and therefore, the stresses and strains are concentrated in the root sectional area. Another complexity is added from the different types of materials used at the root because the GRP blade must be fitted with a steel flange in order to be bolted to the hub flange. The geometry of the root is most complex and does not follow any known rules of construction because an airfoil profile section must be continuously and smoothly coalesced to a circular section at the hub flange. Fortunately, the stress calculations are made for the critical section of the blade root which is circular.

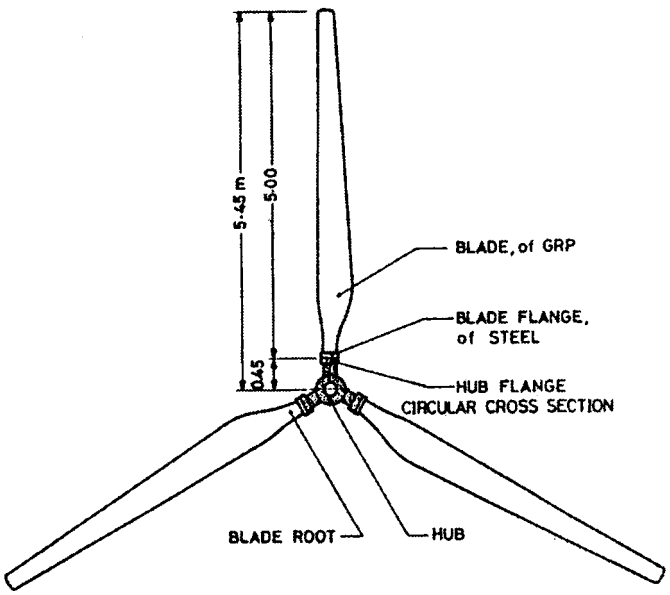

Fig. 5. Three blade rotor assembly showing the hub and the blades.

4.3. Loading conditions

There are no special official design rules for wind turbine blades based on specified loading [12]. The evaluation of the ultimate strength and fatigue characteristics of rotor blade is based on a static proof test [12]. The static proof load is derived from the assumption of an extreme thrust load of $t_{rot} = 300\ N/m^2$ over the swept area. The total load acting on the rotor is then

$$T_{rot} = t_{rot}A_{rot} = (300\ N/m^2)(93.3\ m^2) = 27990\ N$$

This load is equally shared among the three blades and distributed in a triangular pattern from zero at the root center to the maximum value at the tip. This means that each blade of our three bladed rotor should withstand an extreme load of

$$T_{blade} = T_{rot}/B = 27990\ N/3 = 9330\ N = 9.33\ kN/blade$$

The blade should withstand this load without sustaining any damage.

On fatigue, the certification criterion states that at a load factor of $0.5(150 \times A_{rot}/B)$, [12], the measured strain for GRP must be less than 0.2% in the side of the blade under compression and less than 0.3% in the side of the blade under tension. Therefore, we have two load cases:

Case 1: $t_{rot} = 300\ N/m^2$, Load 1 = $(300\ N/m^2)\ (93.3\ m^2)/3$ = 9.33 kN/blade
Case 2: $t_{rot} = 150\ N/m^2$, Load 2 = $150\ N/m^2 \times 93.3\ m^2/3$ = 4.665 kN/blade

(or Load 2 = 0.5 × Load 1 = 0.5 × 9.33 kN/blade = 4.665)

It is understood that the cross section of the root is circular and must be hollow. Therefore, the root has an outer diameter d_o and an inside diameter d_i. Using load Case 1 with the distribution shown in Fig. 6, we obtain $M_{root} = 31.1$ kN m. From Hooke's law, the stress within the root section is:

$$\sigma_{root} = \varepsilon_{root}E_{root} \tag{45}$$

where $E = 30$ GPa is the modulus of elasticity for GRP. With $\varepsilon_{all} = 0.3\%$ in tension and a safety factor of 2, we get:

$$\sigma_{root} = (0.3\%/2)30 \times 10^9\ N/m^2 = 4.5 \times 10^7\ N/m^2 = 45\ MPa$$

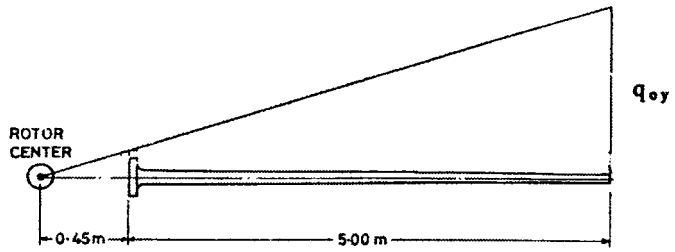

Fig. 6. Load case 1: $P_y = 9.33$ kN and $q_{oy} = 3.424$ N/m for a blade.

Also, from the flexure formula, we have:

$$\sigma_{\text{root}} = \frac{M_{\text{root}} \times r_{\text{root}}}{I_{\text{root}}} \tag{46}$$

With: $I_{\text{root}} = \pi(d_{\text{o}}^4 - d_{\text{i}}^4)$ and $r_{\text{root}} = \frac{d_{\text{o}}}{2}$, Eq. (46) becomes

$$\sigma_{\text{root}} = \frac{32 M_{\text{root}} d_{\text{o}}}{2\pi\left(d_{\text{o}}^4 - d_{\text{i}}^4\right)} \tag{47}$$

or

$$4.5 \times 10^7 \ \text{N/m}^2 = \frac{(158.32 \times 10^3 \ \text{Nm}) d_{\text{o}}}{\left(d_{\text{o}}^4 - d_{\text{i}}^4\right)} \tag{48}$$

Iteration of Eq. (48) yields the required root diameter and root cross sectional area. A practical starting value would be 10% of the blade length. However, it should not exceed the hub diameter. Therefore, we start with $d_{\text{o}} = 0.45$ m and find d_{i} using a small computer program. A graphical solution to Eq. (48) is given in Fig. 7, which also shows the difference between d_{o} and d_{i}, i.e. the thickness of the root. Below $d_{\text{o}} = 0.2$ m, Eq. (48) starts to diverge, and therefore, a minimum outside diameter of $d_{\text{o}} = 0.21$ m and a corresponding inside diameter of $d_{\text{i}} = 0.17$ will be selected. This means that the thickness of the GRP material at the root will be 20 mm.

The root will be fitted with a steel flange to connect the blade to the hub. In order to release the GRP material from stress concentration, the flange will be designed as a jacket like structure from the inside and outside of the blade material as shown in Fig. 8. There are many different alternative solutions to the flange design, but this is outside the scope of this work.

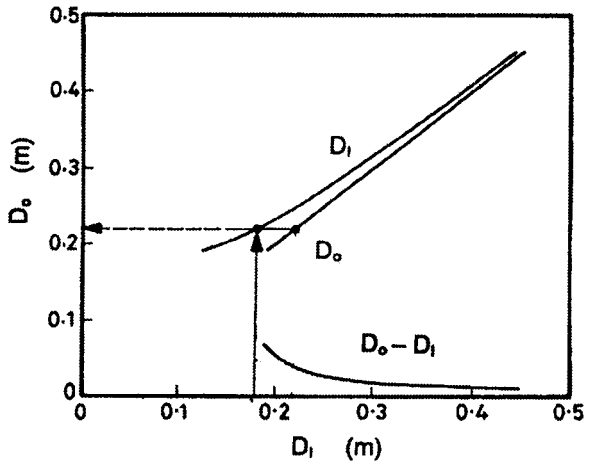

Fig. 7. Determination of outside and inside root diameters.

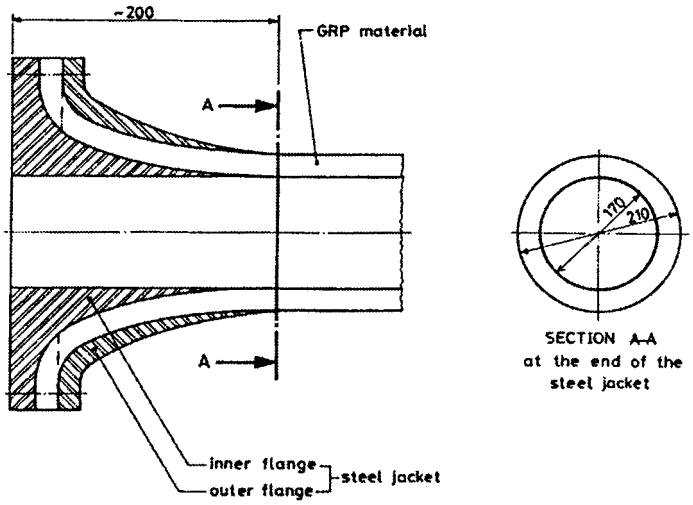

Fig. 8. Design of the blade root.

The important criteria are avoiding sudden changes in geometry and keeping the glass fibers continuous from root to tip.

4.3.1. Blade taper (flapwise)

The blade geometry has two different views, the flapwise view and the edgewise view as can be seen from Fig. 9.

A flapwise view of the proposed blade in Fig. 9a defines the chord length distribution of the selected airfoil over the blade length and also shows the root region and the working region of the blade. The working region is the portion of the blade which has the actual airfoil section,

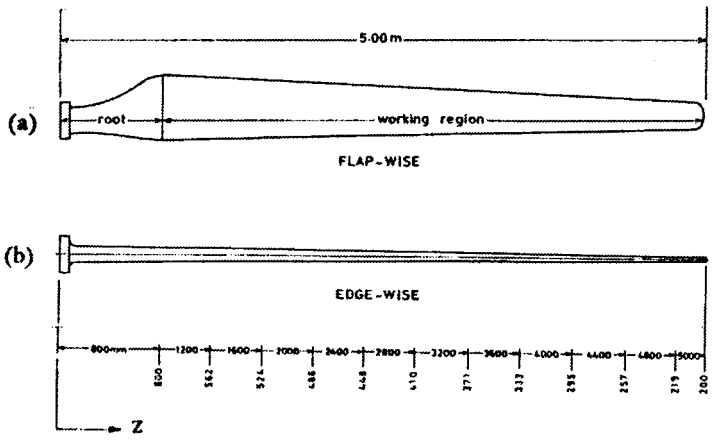

Fig. 9. Viewing the rotor blade geometry: (a) Flap-wise, and (b) Edge-wise.

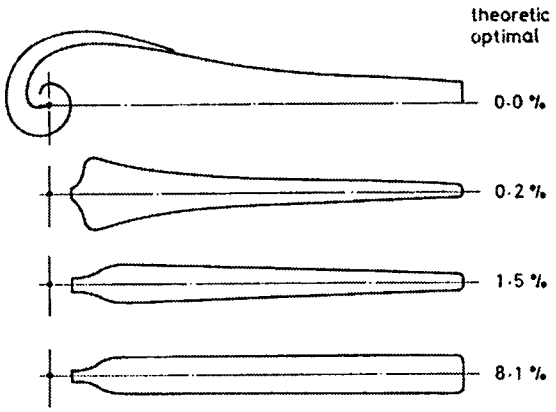

Fig. 10. Efficiency losses related to the ideal blade shape rotor [13].

and the root region is the portion which compensates the geometry between the airfoil profile and the completely circular section at the hub flange and, therefore, does not contribute to power generation. The chord taper of the working region is also chosen linear to simplify manufacturing.

For a streamlined body with the dimensions already calculated and defined for the length, root and tip, the best proportions for the blade, according to Fig. 9a, would be when the chord at the beginning of the working region is 0.6 m and at the tip is 0.2 m. This blade shape would have 1.5% efficiency losses from the theoretical optimum, as shown in Fig. 10, see Ref. [13].

The two acceptable profiles (FX66-S-196 and NACA 63-621) shown in Fig. 4 will have to mix with one another somewhere along the blade length. The mixing must be smooth and, therefore, will be in terms of the two profiles, which requires either scaling up or scaling down. The governing parameter for scaling will be the chord length c and the chord length distribution over the blade length, as shown in Fig. 9a.

4.3.2. Blade thickness (edgewise)

The edgewise view shown in Fig. 9b defines the blade thickness distribution of the selected airfoil over the blade length. The thickest portion of the blade must be the root. Viewing the blade from the edgewise position, one concludes that the blade must be tapered down from the root to the tip for rigidity purposes. The simplest taper is linear, which makes material distribution and manufacturing processes much simpler.

The material thickness at the root is 200 mm at each side, and this must be tapered down to the blade tip. Since the tip must have a finite thickness, a 12 mm thickness will be assigned for each shell, and allowing 1 to 2 mm resin between them gives a total thickness of 25 mm at the tip. The thickness distribution is calculated in terms of the chord, where the total thickness of the blade at any position will be a percentage of the cord length at that position. A thickness distribution envelope for this size of rotor blade is shown in Fig. 11, and therefore the two extreme thicknesses of the blade will be 210 mm at the root and 25 mm at the tip. The thickness distribution must be linear between these two values, and in order to avoid sudden changes, the distribution will be extrapolated, as shown in Fig. 12. The higher point is at the

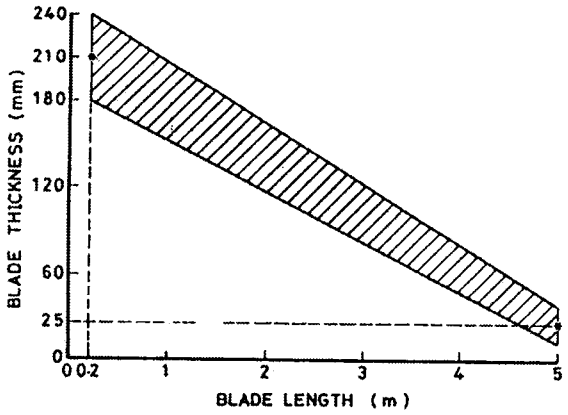

Fig. 11. Envelope of the blade thickness.

edge of the steel flange, where this flange should have a curvature (outward) at the end to avoid stress concentration rises. The lower point, however, cannot fall on the blade because the tip will be chamfered to remove sharp edges for better aerodynamic performance.

4.3.3. Profile mixing (profile matching)

From the profile system designation, the two selected profiles (NACA 63-621) and (FX 66-S-196) have maximum thicknesses of 21 and 19.6% of chord, respectively. In order to match an airfoil profile to any given thickness, the profile thickness is simply multiplied by a certain percentage that makes it match that thickness. In this design, the point of mixing the two profiles was chosen at the beginning of the last third of the blade which should result in a thick blade. At this point, the FX profile will be inserted but with a small percentage which guarantees a smooth transition from the NACA profile.

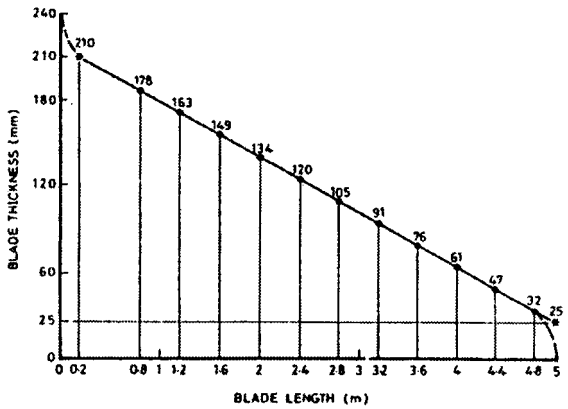

Fig. 12. Distribution of the blade thickness over the blade length.

Table 1
Complete blade data and profile mixing

Station (m)	Chord (mm)	Thickness (mm)	Thickness (%)	Twist (degree)	Profile NACA 63-621 = N21, FXS 66-196 = F196
0.8	600	178	29.7	16.0	1.41 (N21)
1.2	562	163	29.0	12.8	1.38 (N21)
1.6	524	149	28.4	10.1	1.35 (N21)
2.0	486	134	27.6	7.8	1.31 (N21)
2.4	448	120	26.8	5.8	1.28 (N21)
2.8	410	105	25.6	4.2	1.22 (N21)
3.2	371	91	24.5	2.8	0.85 (N21) + 0.34 (F196)
3.6	333	76	22.8	1.8	0.25 (N21) + 0.90 (F196)
4.0	295	61	20.7	0.9	1.06 (F196)
4.4	257	47	18.3	0.4	0.93 (F196)
4.8	219	32	14.6	0.2	0.74 (F196)
5.0	200	25	12.5	0.0	0.64 (F196)

At the next region, however, these percentages will be reversed in favor of the FX profile, and depending on the size of the blade, this transition could be carried on for several positions. The following position then will be purely FX profile with either a scale up or a scale down factor. Table 1 lists the blade parameters with the profile matching sequence.

4.3.4. Twist of the blade

The twist of the blade is defined in terms of the chord line. Blade twist angle is a synonym for the pitch angle, however the twist defines the pitch settings at each position along the blade according to local flow conditions. From the velocity triangle in Fig. 3 and as explained by Habali and Saleh [14], the pitch angle β is large near the root, where the rotational speed (is $V_t = r\Omega$) low and small at the tip where the rotational speed is high. This situation suggests a match between the twist and rotational speed, since the relative wind velocity W is

$$W = U + \Omega r \tag{49}$$

Here is a decision to be made:

- fixing Ω and searching for the optimum twist β, or
- fixing β and searching for the optimum Ω.

The first choice is better because it is easier for designing the gear and the generator. Ω was chosen to be 75 rpm. As a first estimate of the twist, we use the equation for twist of the zero lift line:

$$\beta = ((R\alpha_t/r) - \alpha_t) - k(1 - r/R) \tag{50}$$

where α_t is the angle of attack at the tip and k is a constant such that $k > 0$. α_t can be calculated from the velocity triangle shown in Fig. 3 as follows: knowing that $\Omega = 75$ rpm $= 2\pi \times 75/60$ s $= 7.8575$ 1/s, we obtain a rotational tip speed of $V_t = R\Omega = 39.27$ m/s. Taking a mean free stream wind speed of $U = 7$ m/s, which is usually taken as a design wind speed [7],

then from Fig. 3, we get $\Phi = \tan^{-1}(7/39.2) = 10.1^\circ$. Since $0^\circ \le \beta_t \le 2^\circ$, taking $\beta_t = 2$, gives $\alpha_t = \Phi - \beta = 8.1^\circ \approx 8^\circ$. For $\alpha_0 = -2^\circ$, α_t becomes 6°, and with Eq. (50) and a wide band of zero lift, the twist can be produced for a range of k values, as shown in Fig. 13.

From the design point of view, only the twist distribution that produces the required power level at $\Omega = 75$ rpm will be selected. Thus a question of how much the rotor should be loaded, where a generator size can be chosen, and then one can see how much the rotor is really loaded.

5. Calculation of wind turbine power output

The procedure to calculate the wind turbine output using airfoil data was first established by Wilson and Lissaman [7], and it is shown in detail by Saleh [15]. He used some program packages, such as PROP, SEA and AERODYN™. Table 1 shows the complete blade data and some results calculated by using AERODYN™.

From Table 2, we see that the power level is very close for the four twist distributions, and by each twist the power increases nonlinearly with the wind speed. For the fast running blades, the smallest one (16° distribution) for the wind speed of 10 m/s will be chosen, which fits a generator output of 15 kW as follows: $P(10) = 19.03$ kW, with a gearbox efficiency of $\eta_m = 0.93$, and a generator efficiency of $\eta_e = 0.85$, the overall power will be the rated power: $P_{rat} = P(10) \times \eta_m \times \eta_e = 19.03 \text{ kW} \times 0.93 \times 0.85 = 15.05$ kW. This concludes the determination of the blade data and the geometry of the blade is then completely defined which will allow determination of the blade loads and other aerodynamic characteristics.

6. Stress analysis of the blade

The blade geometry obtained previously is one of the most complex shapes encountered in engineering problems. A blade combined of different airfoil sections at different geometric positions with different twists, thicknesses and chords is extremely difficult to analyze.

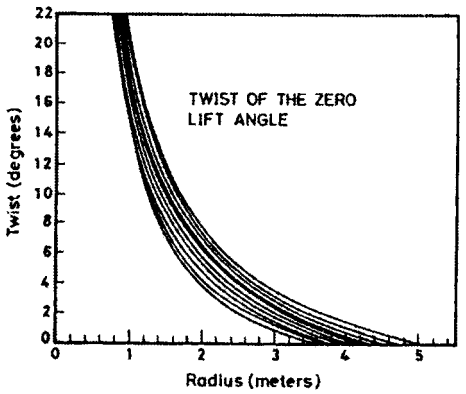

Fig. 13. Graph of the zero-lift line.

Table 2
P (4 m/s), P (10 m/s), and P (16 m/s) for the four-twist distributions

Twist (degree)	rpm	Pitch (degree)	P (4) (kW)	P (10) (kW)	P (16) (kW)
22	75	0.0	1.06	20.13	23.38
20	75	0.0	1.00	19.45	21.95
18	75	0.0	0.98	19.50	21.11
16	75	0.0	0.98	19.03	21.22

Therefore, an approximate solution using the Finite-Element Method (FEM) will be an ultimate choice of solution.

6.1. Blade aerodynamic forces (blade loadings)

The blade geometry obtained previously forms the main data necessary to formulate a model in order to calculate the aerodynamic forces and other data, such as the operating parameters. The procedure for calculating the aerodynamic blade loadings is shown in detail by Saleh [15]. For these calculations, the programs:

- LOADS (developed at Oregon State University in 1980 to analyze blade loads for rigid rotors of simple geometry including flapwise flexing and unsteady aerodynamics, without yawing and without pitch variations), see Ref. [1].
- YawDyn for yaw considerations [16], and
- MOSTAB, SEACC and AERODYN

were used. The data input to the program will be the blade geometry, as shown in Table 1, and the programs will be run for a range of wind speeds and pitch angle, in addition to twelve different yaw positions. Table 3 gives the values of the force and moment components acting on the blade during operation at a maximum wind speed of 25 m/s and zero-pitch angle ($\beta = 0$). Fig. 14 shows all loading types acting on the flying blade.

The shear force V_y and the bending moment m_x are the dominant components, and, therefore, will be studied at different settings of pitch angles ($0^\circ \leq \beta \leq 40^\circ$). Table 4 shows the maximum shear forces and the maximum bending moments for a maximum operating wind speed of 25 m/s and a pitch angle range extending from 0° to 40° in increments of 4°. The rotational speed of the rotor is $\Omega = 75$ rpm. It can be seen from these tables that the shear force V_y and the bending moment m_x reach their maximum values near the blade root for vanishing pitch angle. Much higher loads would occur if the wind is blowing at a skew angle relative to the blade, which is called the yaw effect. Another computer run was made to calculate the loads resulting from 30 yaw angle, which is considered as the maximum skew encountered during continuous operation.

6.2. Blade reaction forces

For stress analysis purposes, only the force distribution per length (flapwise) will be calculated because this force represents the maximum load in the most critical direction.

Table 3
Blade loads and moments along the blade during normal operation at a maximum wind speed of 25 m/s and zero pitch angle

Radial position (m)	Forces and moments						
	q_x (N/m)	q_y (N/m)	V_x (N)	V_y (N)	m_x (Nm)	m_y (Nm)	m_c (Nm)
0.00	0.00	0.00	335	1561	1055	5286	0.00
1.25	140	320	355	1561	612	3334	3374
1.95	115	346	266	1329	397	2326	2359
2.61	97	373	196	1091	245	1523	1542
3.23	83	394	140	855	142	923	931
3.78	71	401	98	633	76	508	511
4.27	63	400	65	473	36	246	246
4.69	57	391	40	273	15	99	99
5.02	53	374	22	147	4	30	30
5.26	52	359	9	60	1	5	5
5.40	54	344	1	8	0	0	0
5.45	0	0	0	0	0	0	0

Furthermore, according to the German DIN, blade loads shall be calculated at an extreme gust of 42 m/s speed. Table 5 shows thrust load (q_y) and drag load (q_x) distributions over the blade length for 25 and 42 m/s wind speeds, respectively, and 30° yaw and zero pitch angles. This load distribution is plotted in Fig. 15 to show the loading configuration during the maximum operating conditions. The area under the curves was also graphically integrated to identify the total loads. It is noticed that the reactions to the total load under the 42 m/s curve, i.e., the F_y (42 m/s) load, represents the load Case 2 studied previously.

6.3. Properties of the blade

6.3.1. Material-mechanical properties

The used material is assigned as GRP material with the mechanical properties given in Table 6.

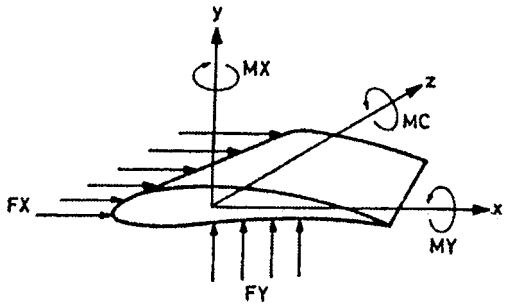

Fig. 14. Aerodynamic loads and moments.

Table 4
Maximum shear forces V_y and maximum bending moment m_x for different pitch angles β

Radial position $r = z$, (m)	V_y (N) and m_x (Nm)	Pitch angle settings β (degree)										
		0	4	8	12	16	20	24	28	32	36	40
0.0	V_y	1561	1497	1440	1392	1347	1314	1255	1115	893	619	0
	m_x	5286	5079	4914	4791	4673	4604	4378	3767	2832	1737	807
1.25	V_y	1561	1497	1440	1392	1347	1314	1255	1115	893	619	0
	m_x	3334	3207	3114	3051	2989	2962	2809	2374	1716	964	372
1.95	V_y	1329	1276	1231	1197	1168	1148	1099	971	760	485	170
	m_x	2326	2240	2182	2148	2111	2102	1987	1645	1138	577	168
2.61	V_y	1091	1048	1016	996	978	966	926	809	596	338	153
	m_x	1523	1469	1438	1420	1400	1401	1315	1054	687	304	48
3.23	V_y	855	823	803	793	781	755	746	626	423	209	111
	m_x	923	893	877	869	857	864	799	611	373	163	−4
3.78	V_y	633	612	601	597	586	589	561	437	273	110	57
	m_x	508	492	485	481	475	484	433	314	179	48	−15
4.27	V_y	437	423	418	415	407	417	381	276	159	45	0
	m_x	246	239	236	232	232	237	202	140	74	11	−11
4.69	V_y	273	266	262	259	256	266	226	155	81	11	−9
	m_x	99	96	95	93	95	95	77	51	25	1	−5
5.02	V_y	147	143	142	138	141	142	113	74	35	−1	−17
	m_x	30	29	29	28	29	28	22	14	6	−1	−2
5.26	V_y	60	58	58	56	60	55	42	27	12	−2	−21
	m_x	5	5	5	5	5	5	3	2	1	0	0
5.40	V_y	8	8	8	8	9	7	6	3	1	0	−21
	m_x	0	0	0	0	0	0	0	0	0	0	0
5.45	V_y	0	0	0	0	0	0	0	0	0	0	0
	m_x	0	0	0	0	0	0	0	0	0	0	0

Table 5
Blade loads q_x (N/m) and q_y (N/m) distributions for: 25 and 42 m/s wind speeds and 30° yaw and 0° pitch angles

Radial position $R = z$, (m)	q_y (25 m/s) (N/m)	q_x (25 m/s) (N/m)	q_y (42 m/s) (N/m)	q_x (42 m/s) (N/m)
0.00	0.0	0.0	0.0	0.0
1.25	395	200	908	414
1.95	468	182	996	336
2.61	531	166	1047	276
3.23	578	152	1062	227
3.78	603	139	1043	189
4.27	611	130	1003	162
4.69	598	121	948	142
5.02	557	107	886	129
5.26	531	103	833	123
5.40	513	109	791	124
5.45	0.0	0.0	0.0	0.0

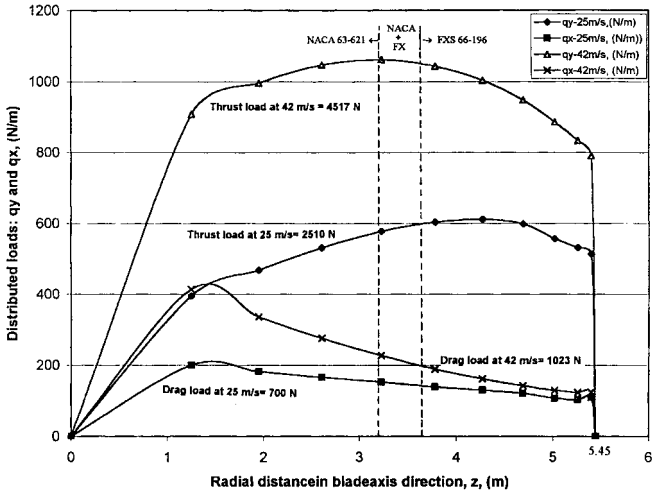

Fig. 15. Configuration of load distribution for 25 and 42 m/s wind speeds.

6.3.2. Blade-mass properties

The blade-mass properties are calculated and given in Table 7. The second moments of area ($Ix(z)$ and $Iy(z)$) distribution over the blade length is shown in Fig. 16. Furthermore, the four critical sections of the blade are shown in Fig. 17.

6.4. Finite element modeling

6.4.1. Geometric solid modeling

In order to utilize FEM, a solid model for the blade must be created first to define the surface boundaries and domain contained in it. The contained domain will determine the shape and the number of elements that could be used in the analysis. The solid model is created in ARIES in three steps as mentioned by Saleh [15]. One of the most powerful solid modelers is the ARIES Mechanical Computer Aided Engineering Design (MCAED) software used by the Renewable Research Center (RERC) at the Royal Scientific Society. This package was

Table 6
GRP mechanical properties

Density	$\rho = 1.4 \times 10^{-6}$ kg/mm^3
Tensile yield strength	$\sigma_{yt} = 63$ MPa
Ultimate tensile strength	$\sigma_u = 129$ MPa
Modulus of elasticity	$E = 6$ GPa
Compressive strength	$\sigma_{yc} = 170$ MPa
Shear modulus	$G = 2.5424$ GPa
Poisson's ratio	$\nu = 0.18$
Glass content	$c = 50\%$

Table 7
Blade mass properties

Weight = 1156.87 N	Mass = 117.97 kg	
Volume = 8.4263×10^7 mm^3	Density = 1.4×10^{-6} kg/mm^3	
Area = 7.4522×10^6 mm^2		
Properties with respect to origin at the hub		
$O_x = 0.0$	$O_y = 0.0$	$O_z = 0.0$
Mass moment of inertia (kg/mm^2)		
$I_x = 2.544 \times 10^8$	$I_y = 2.560 \times 10^8$	$I_z = 2.172 \times 10^6$
Center of gravity (mm)		
$C_{gx} = 44.27$	$C_{gy} = 17.59$	$C_{gz} = 1668$
Root cross sectional area properties		
$A_{\text{root}} = 18800$ mm^2	$I_{x,\text{root}} = 70.844 \times 10^6$ mm^4	$I_{y,\text{root}} = 55.374 \times 10^6$ mm^4

developed by ARIES Technology in Lowell, Massachusetts, USA, for mechanical engineering design and analysis. The FEM model consists of three phases, as shown in Fig. 18 and in Aries Technology (1993) [17]. The modeling is the preprocessing phase of the finite element process, which includes geometry creating, definitions of loading and restraining conditions and constructing of an efficient mesh.

Taking the maximum loads on the blade at 42 m/s from Table 5 and Fig. 15, we get a maximum thrust load (flapwise) of $F_{y,\text{root}} = 4.82$ kN applied at the aerodynamic center of the blade, which is located at $0.5L_b = 0.5 \times 5.45$ m $= 2.725$ m. Then, at the root section, we have:

- the thrust force $F_{y,\text{root}} = 4.517$ kN,
- the moment $M_{x,\text{root}} = 4.82$ kN $\times$ 2.5333 m $= 11.443$ kN m,
- the drag force $F_{x,\text{root}} = 1.023$ kN, and
- the moment $M_{y,\text{root}} = 1.023$ kN $\times$ 2.5333 m $= 2.592$ kN m.

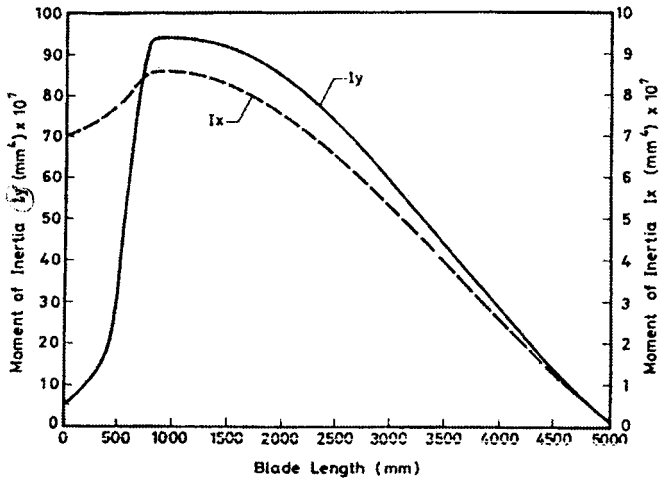

Fig. 16. Distribution of second moments of inertia I_x and I_y along the blade.

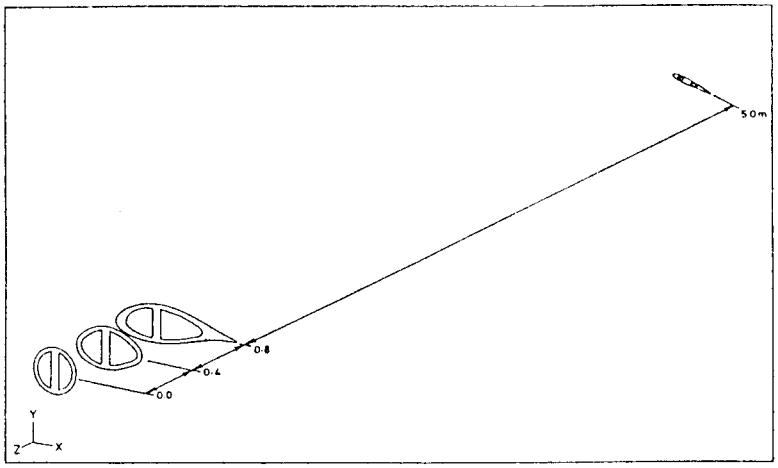

Fig. 17. Minimum number of section curves for the blade.

Furthermore, the blade is subjected to a centrifugal force F_c due to its rotational motion. The centrifugal force is a function of z (coordinate of the blade length) and can be calculated at each z from the formula:

$$F_c(z) = \frac{\Omega^2 \rho A(z)(L^2 - z^2)}{2} \tag{51a}$$

which shows that the maximum centrifugal force, $F_{c,max}$, occurs at the root ($z = 0$),

$$F_{c,max} = F_c(0) = \frac{\Omega^2 \rho A(0) L^2}{2} = 20.3 \text{ kN} \tag{51b}$$

At this point, the geometry, the restraint and the load conditions are all available. The root

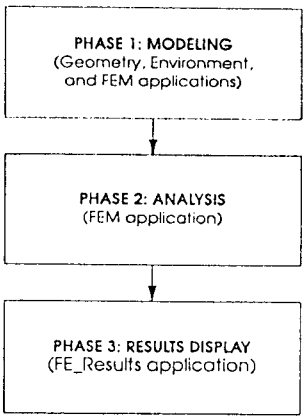

Fig. 18. Phases of FEM modeling of the rotor blade.

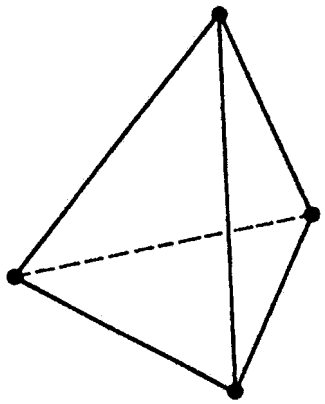

Fig. 19. Tetrahydron element of four nodes with three degrees of freedom (u_x,u_y,u_z) per node.

region geometry is meshed using a TETRAHYDRON element of four nodes and three degrees of freedom at each node (u_x,u_y,u_z), see Fig. 19. The modeled region contains 1103 nodes and 3867 elements. The model, at this point, is considered complete and ready to be submitted to the built-in module of the well known FE package ANSYS within ARIES in order to be analyzed. This is the second phase of the FE modeling which is the processing phase. Fig. 20 shows the forces at the root region as a computer output.

The third and the last phase of the FE modeling is the results display which is the post processing phase. The most important output required here is the displacements and stresses resulting from the applied loads. Fig. 21a shows the forces and the moments whereas Fig. 21b shows the stress distribution at the root section.

7. Results and discussion

7.1. Stress, strain and deflection

The results of the analysis using FEM are displayed after completing the calculation. The results indicate a maximum (principal) stress of $\sigma_{max} = 9.348$ N/mm^2 = 9.348 MPa occuring at the tension side of the root cross section of the blade. Comparing this stress with $\sigma_{y,GRP} = 63$ MPa gives a factor of safety of 6.7. This principal stress is also compared with the root stress $\sigma_{root} = 45$ MPa calculated previously for a factor of safety of 2. The difference between the two results (σ_{max} and σ_{root}) is due to the centrifugal and drag forces added to the model by the FE analysis and the additional cross sectional area at the root section represented by the rectangular spar at the blade center. The stress distribution over the blade length is difficult to be plotted since each fiber has its own stress distribution. Generally, we can say the stress σ_z shows a decreasing nonlinear variation over the blade length. However, the stress distribution over the root cross section is shown in Fig. 21b.

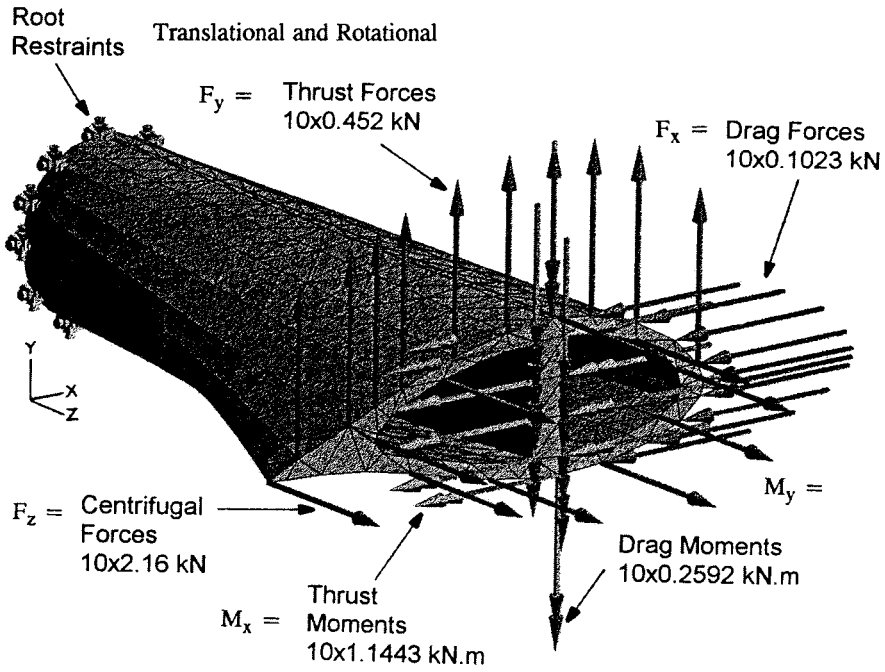

Fig. 20. Complete FE model of the blade-root region by ARIES™.

The strain at the most lower fiber which suffers maximum tension is $\varepsilon_{\text{lower}} = \varepsilon_{\max} = 0.15\%$, and according to the certification criteria of Jensen [12], this is below the allowable strain, $\varepsilon_{\text{all}} = 0.3\%$.

The blade deflection distribution over the blade length is shown in Fig. 22. The maximum calculated deflection at the blade tip is $u_{y,\text{tip}} = 104.3$ mm under the given loads, which

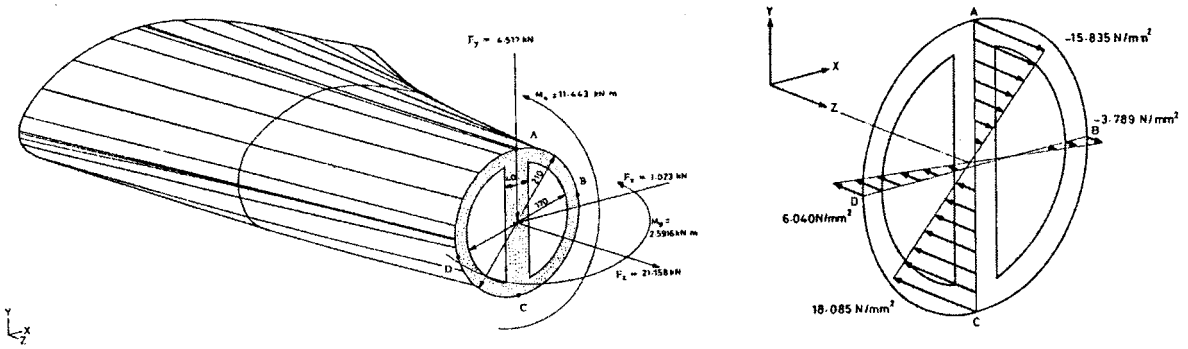

Fig. 21. Blade root cross section with: (a) loads and moments imposed, and (b) stress distribution.

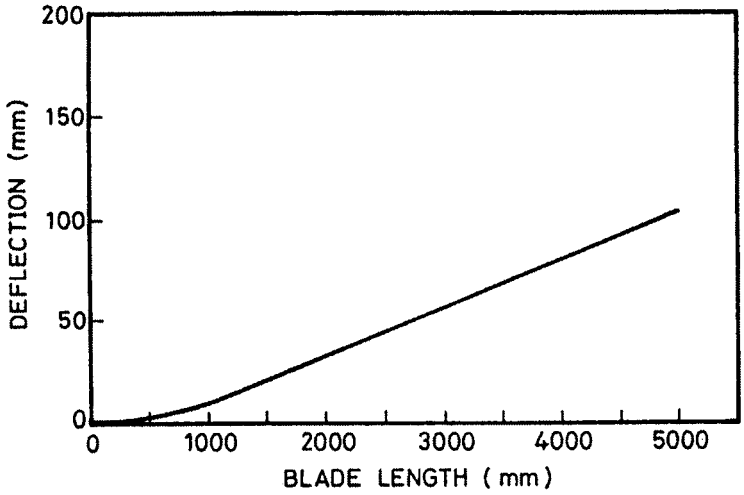

Fig. 22. Curve-fit extrapolation of blade deflection (u_y) during extreme operating conditions at 42 m/s wind speed.

concludes the analysis by insuring enough margin for safety of the design especially during extreme operating situations.

In order to analyze the FEM solution, simple straight forward bending strength calculations will indicate its accuracy. This is accomplished through using the flexure formula for the combined loadings

$$\sigma_z(x,y,z) = \frac{F_c}{A_z} \pm \frac{M_y x}{I_y} \pm \frac{M_x y}{I_x} \tag{52}$$

where the positive sign corresponds to tension and the minus sign to compression. The root cross section shown in Fig. 21a has the properties:

$$I_{x,\text{root}} = \frac{\pi\left(d_o^4 - d_i^4\right)}{64} + \frac{bh^3}{12} = 70.8440308 \times 10^6 \ \text{mm}^4$$

$$I_{y,\text{root}} = \frac{\pi\left(d_o^4 - d_i^4\right)}{64} + \frac{hb^3}{12} = 55.374030 \times 10^6 \ \text{mm}^4$$

and

$$A_{z,\text{root}} = 18800 \ \text{mm}^2.$$

Thus, Eq. (52) provides the stress distribution over the root cross section:

$$\sigma_{z,\text{root}}(x,y) = +1.0798 \pm 4.9142x \pm 16.9600y$$

The sense of the forces and moments shown in Fig. 21a determines the signs of the stresses. This stress represents a complex surface that extends over the root cross sectional area. Therefore, the outer-most fiber stresses at points A, B, C and D of the root cross section, shown in Fig. 21b, are:

$$\sigma_A = -15.835 \text{ MPa}$$

$$\sigma_B = -3.789 \text{ MPa}$$

$$\sigma_C = +18.085 \text{ MPa}$$

$$\sigma_D = +6.040 \text{ MPa}.$$

The maximum tensile stress is $\sigma_C = 18.085$ MPa occuring at point C, which is much lower than $\sigma_{\text{yt,GRP}} = 63$ MPa with a factor of safety of 3.5. The maximum compressive stress is $\sigma_A = 15.835$ MPa occurring at point A, which is much lower than $\sigma_{YC,\text{GRP}} = 170$ MPa, with a factor of safety of 10.7.

The results obtained by the FEM solution gave the maximum (principal) stress as 9.3487 MPa which certainly falls within the stress distribution shown in Fig. 21b. The reason for the difference between the FEM results and the foregoing analysis results is that in the later one, concentrated load representation was used at the root to represent the actual distributed aerodynamic loads.

From the previous discussion, two conclusions can be obtained:

1. The FEM solution is satisfactory and acceptable.
2. The blade material for the given root design can withstand the applied loads with enough safety margin.

8. Conclusions and recommendations

- Rotor inertia has a great effect on power production, where during start up before reaching the cut in speed, the rotor requires higher torque to start turning and production but much less torque is needed to produce the same unit power after it has run up to full speed.
- The necessary data for evaluation of the rotor blade performance can be produced by the results of measurements. The power curve is the most important piece of information. For a pitch regulated wind turbine, the performance of this design of GRP blades can only be seen in the part of the power curve up to the rated power of 15 kW at 10 m/s. Beyond this point, the performance of the blade is overshadowed by the control system which dumps all excess power (over the rated), thereby indicating a decrease in efficiency as indicated by the C_p–λ curve.
- The wind shear (horizontal or vertical) has also an effect on the strength of the blade. This effect is more clear with large rotors, but it still has a markable influence on small turbines.

- For a fully satisfactorily analysis using the FEM, large computers with very advanced software have to be used. Automatic mesh generation and satisfactory solutions have to be examined.
- For fully understanding the mechanical behaviour of the rotor blades, tests should be performed by conducting a thorough fatigue test program, which is usually characterized by being costly and time consuming.
- Since the blade root exhibited durability and resilience during testing and operation, it is recommended that the design of the blade root be more theoretically investigated using the theory of elasticity for anisotropic composite materials in three dimensions.
- It is recommended that other profiles and other composite materials for other wind regimes be studied.

References

[1] Harten JR. Evaluation of prediction methodology for blade loads on a horizontal axis wind turbine. In: Ninth ASME Wind Energy Symposium, SED-9:. New Orleans, LA, January 14–18. 1990. p. 105–10.
[2] Park J. Simplified wind power systems for experimentation. Brownsville, CA: Hellion Inc, 1975.
[3] Jackson KL, Migliore PG. Design of wind turbine blades employing advanced airfoils. In: West Wind Industry, Inc., Windpower-87 Conference. San Francisco, CA, October. 1987.
[4] Lysen EH. In: 2nd ed, Introduction to wind energy, CWD 82-1. Netherlands: Amersfort, 1983.
[5] Tangler J, Smith B, Jager D, Olson, T. Atmospheric performance of the special-purpose SERI thin-airfoil family, Final results. Solar Energy Research Institute, 1817 Code Blvd., Golden, CO., Presented at ECWEC 90, Madrid, 1990.
[6] Davidson R. Danes to test run new american blades. Windpower monthly.
[7] Wilson RE, Lissaman PBS. Applied aerodynamics of wind power of wind power machines. National Science Foundation. Under Grant No. GI-41840, Oregon State University, OR, May, 1974.
[8] Prandtl L. Appendix to wind turbines with minimum energy losses. In: Betz A, editor. Goettenger News, Goettenger, 1919, pp. 193–217.
[9] Miley SJ. A catalog of low Reynolds number airfoil data for wind turbine applications, USDOE, Wind Energy Tech. Division, Report-3387, UC-60, February, 1982.
[10] Mikhail AS. Wind power for developing nations. USDOE, Wind Tech. Division, SERI/ TR-762-966, UC Category: 60, July, 1980.
[11] Ta'ani R, Amr M, Saleh I. Water pumping from deep wells by using Aeroman 12.5/14 wind energy converter. In: 16th International Sonnenforum, Berlin 2. DGS-Sonnenenergie Verlag GmbH, Muenchen, Germany, August 22–September 2. 1988.
[12] Jensen PH. Static test of wind turbine blades. Test station for wind mills, Risoe National Laboratory, Roskilde, Denmark, April, Jensen PH, Krogsgaard J, Lundsger P, Rasmussen F. Fatigue testing of wind turbine blades. EWEA Conference and Exhibition, Rome, Italy, October, 1986.
[13] Moment R, Pastore J. Wind energy conversion. In: A Short Seminar Presented to the Royal Scientific Society by Rocky Flats Wind Energy Research Center, Rockwell International Corporation, USAID, March. 1984. p. 10–4.
[14] Habali SM, Saleh IA. Pitch control criteria for small wind turbines. In: Proceedings of the 1992 International Renewable Energy Conference, 2:. University of Jordan, Amman, Jordan. 1992. p. 459–559.
[15] Saleh I. Testing and performance of locally manufactured glass fiber wind turbine blade. Master thesis, College of Engineering and Technology, University of Jordan, Amman, Jordan. March, 1994.

[16] Hansen AC, Cui X. A summary of experiences in the analysis of rigid rotor yaw control systems. In: Ninth ASME Wind Energy Symposium. SED-9:. ASME, NY, January. 1990. p. 181–7.
[17] Aries Technology, Inc. Finite element modeling reference manual, P/N2806301, Aries Technology, Inc., 600 Suffolk Street, Lowell, Masschusetts 01854, 1993.